The Seismic Record
A journal of the Seismological Society of America

An Enhanced Focal Mechanism Catalog of Induced Earthquakes in Weiyuan, Sichuan, from Dense Array Data and a Multitask Deep Learning Model

OPEN ACCESS

Junhao Song[1,2], Weiqiang Zhu[2], Jinping Zi[3], Hongfeng Yang[*1,3], and Risheng Chu[4]

Abstract

Determining focal mechanisms of abundant small-magnitude (M < 3) earthquakes can better reveal subsurface fault structures and stress features, but it remains challenging due to insufficient records or inefficient methods. In the past decade, seismicity in the Weiyuan region of the southern Sichuan basin has increased dramatically following massive hydraulic fracturing activities. Here, we apply a multitask deep learning model, PhaseNet+, to local dense seismic records to enhance the focal mechanism catalog. 38,518 earthquakes are first detected and well located using predicted phase arrivals and the improved 1D velocity models. From predicted *P* polarities and measured *S/P* ratios, 20,740 focal mechanisms of varying qualities are then computed. Among 4399 high-quality focal mechanisms, about 92% are primarily associated with reverse faulting. It agrees well with moment tensor focal mechanisms from previous studies and the local tectonic settings, suggesting that the enhanced catalog can provide reliable faulting mechanisms. We observe clear spatial perturbations in their P-axis azimuths, mainly associated with variations in fault strikes. Nevertheless, changes in the stress field at short-length scales are also obvious, likely caused by intersected fault structures. Recent fluid injection operations and moderate earthquakes in Weiyuan may have further altered the subsurface stress state, demanding more detailed investigations.

Cite this article as Song, J., W. Zhu, J. Zi, H. Yang, and R. Chu (2025). An Enhanced Focal Mechanism Catalog of Induced Earthquakes in Weiyuan, Sichuan, from Dense Array Data and a Multitask Deep Learning Model, *The Seismic Record*. **5**(**2**), 175–184, doi: 10.1785/0320250004.

Supplemental Material

Introduction

Earthquake focal mechanisms provide important information for analyzing subsurface fault zone geometries, rupture kinematics, and crustal stress fields (e.g., Cheng *et al.*, 2023; Shelly *et al.*, 2023). Focal mechanisms of moderate-to-large earthquakes are generally determined by inverting low-frequency waveforms (e.g., Yang *et al.*, 2020) or coseismic deformations (e.g., Zhang *et al.*, 2024). But for smaller earthquakes (M < 3), which occur more frequently, waveform-based inversion of focal mechanisms is more difficult due to insufficient high signal-to-noise ratio (SNR) records. Furthermore, smaller earthquakes tend to generate higher-frequency waveforms that are more susceptible to smaller-scale material heterogeneities, hindering the match between synthetics and observations (e.g., Li *et al.*, 2011). As a result, small earthquake focal mechanisms are usually inverted with other constraints such as first-motion polarity and *S/P* amplitude ratio (Hardebeck and Shearer, 2002, 2003). In recent years, the determination of first-motion polarity has been greatly facilitated by novel techniques such as deep learning-based polarity classifiers (e.g., Ross *et al.*, 2018) or relative polarity

1. Department of Earth and Environmental Science, The Chinese University of Hong Kong, Shatin, Hong Kong, China, https://orcid.org/0000-0003-2706-0778 (JS); https://orcid.org/0000-0002-5925-6487 (HY); 2. Department of Earth and Planetary Science, University of California, Berkeley, California, U.S.A.; 3. Shenzhen Research Institute, The Chinese University of Hong Kong, Shenzhen, China, https://orcid.org/0000-0002-0891-8305 (JZ); 4. State Key Laboratory of Precision Geodesy, Innovation Academy for Precision Measurement Science and Technology, Chinese Academy of Sciences, Wuhan, China, https://orcid.org/0000-0002-1062-5982 (RC)

*Corresponding author: hyang@cuhk.edu.hk

estimated by the cross-correlation technique (e.g., Shelly *et al.*, 2016). Benefiting from such advancements, refined focal mechanism catalogs consisting of many smaller earthquakes have constrained fault structures and stress states at higher spatiotemporal resolutions (e.g., Shelly *et al.*, 2023).

The Weiyuan region, located in the southern Sichuan basin (Fig. 1), is one of China's largest shale gas fields. In the past decade, seismicity has dramatically increased following massive hydraulic fracturing activities in Weiyuan, including a few damaging events (e.g., Yang *et al.*, 2020; Zhang *et al.*, 2024). Previous investigations of their spatiotemporal variations suggest that these induced earthquakes occurred mainly on pre-existing faults reactivated by fluid injection and diffusion activities from nearby wells (e.g., Sheng *et al.*, 2022). Other triggering mechanisms such as stress perturbation resulted from postinjection aseismic slip have also been proposed through numerical experiments to explain the observed migration patterns (e.g., Zi *et al.*, 2025). To better understand the mechanisms behind induced earthquakes and mitigate seismic hazards in this region, deriving detailed source parameters and subsurface stress states is an important task. Focal mechanisms of earthquakes with magnitudes larger than 3 have been well investigated using the waveform fitting method (Yi *et al.*, 2020). Benefiting from a local dense array, Chu and Sheng (2023) determined focal mechanisms of 257 earthquakes with M > 1.5, although the waveforms of small earthquakes (M < 1.8) did not fit the synthetics equally well compared to those of larger events.

In this study, we aim to compile an enhanced focal mechanism catalog in the Weiyuan region by constraining small earthquake focal mechanisms with first-motion polarity and *S*/*P* amplitude ratio measurements. We first apply a multitask deep learning model (Zhu *et al.*, 2025) to seismic data of the dense temporary array used by Chu and Sheng (2023). We then build a high-resolution catalog of 38,518 hypocenters as well as their uncertainties using predicted phase arrivals and refined 1D velocity models. Finally, 20,740 focal mechanisms with varying qualities are inverted, and 4,399 good-quality solutions are selected for further analysis. The results exhibit finer-scale variations in fault structures and tectonic stress, demonstrating the great efficiency of the adopted workflow in determining earthquake focal mechanisms from large amounts of seismic records.

Data and Methods

Dense array and velocity models

The dense array used in this study consists of 50 temporary stations deployed over the northeast Weiyuan area from November 2015 to November 2016 (Fig. 1). It provided good coverage of active hydraulic fracturing wells during this period with an average station spacing of ~5 km and captured abundant induced seismicity (e.g., Zhou *et al.*, 2021). Each station was equipped with the Güralp CMG-40T seismograph, recording three-component ground velocities with a sampling rate of 100 Hz and flat response above 0.5 Hz (Chu and Sheng, 2023). 1D *P*- and *S*-velocity models extracted from finer scale subsurface velocity structures beneath the dense array, which were inverted by double-difference seismic tomography (Zi *et al.*, 2023), are used for later phase association and earthquake location. In the focal mechanism inversion step, we include another 1D V_P model from Zhou *et al.* (2021) to consider variations and imperfect knowledge in velocity structures. For ease of reference, we name them the ZiVp1D, ZiVs1D, and ZhouVp1D models (Fig. S1, available in the supplemental material to this article).

Earthquake detection and location

We use PhaseNet+ (Zhu *et al.*, 2025), a multitask deep learning model built upon PhaseNet (Zhu and Beroza, 2019), to simultaneously predict event origin time, phase arrival time, and phase onset polarity (Fig. 2a,b). We obtain ~1.61 million *P* and ~1.54 million *S* arrivals with a minimum score of 0.5. We then adopt the GaMMA method (Zhu *et al.*, 2022), faster than most grid-searching-based methods, to associate picks into individual events. The maximum time separation between two neighboring picks (*dbscan_eps*) is set as a relatively large value of 5 considering that some stations failed to operate toward the end of deployment and led to larger interstation spacings (Sheng *et al.*, 2022). We associate ~2.15 million picks into 155,532 events by requiring at least 5 picks (either *P* or *S*) per event (Fig. S2). Because our objective is to compile a catalog of double-couple focal mechanisms, we only focus on those events most likely related to the shear failures. Therefore, we retain 38,865 events associated with at least 8 *P* and 8 *S* phases and then refine their locations using HYPOINVERSE (Klein, 2002). Finally, we build a hypocenter catalog of 38,518 earthquakes after removing those with time residuals (root mean square of travel-time residual) larger than 0.1 s, or horizontal uncertainties greater than 0.5 km, or vertical uncertainties greater than 1.0 km (Fig. 1). The absolute locations and corresponding uncertainties are used for inverting focal mechanisms in the next section. To better delineate the fault structures, their relative locations are further inverted with HypoDD (Waldhauser and Ellsworth, 2000) based on the catalog travel

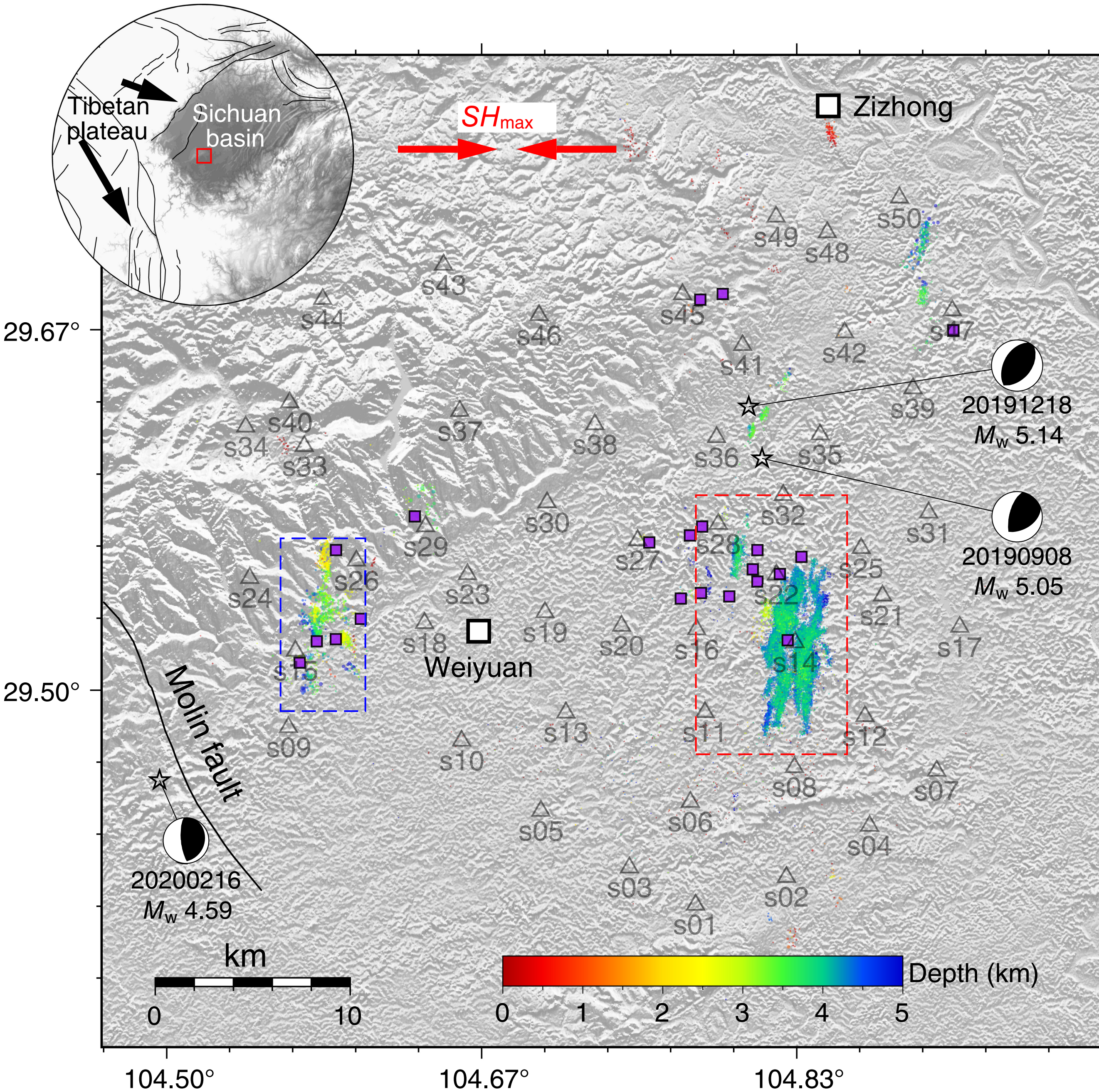

Figure 1. Map of the study region. The black triangles indicate dense seismic stations with their names below. Local seismic events detected and well-located in this study are colored by their hypocenter depths. The west and east clusters are highlighted by blue and red dashed boxes. The purple squares denote the locations of hydraulic fracturing well pads. The black line marks the Molin fault. The red arrows denote the approximate orientation of the local maximum principal stress in this area. The black stars mark three moderate earthquakes that caused surface deformation together with their focal mechanisms determined in Zhang *et al.* (2024). The inset map shows the location of the Weiyuan region and its brief tectonic background. The black thin lines delineate active faults, and thick arrows indicate the overall movements of crustal materials.

time and cross-correlation differential time. The association, location, and relocation results can be found in Figures S2–S4.

Focal mechanism inversion

The predicted polarity ranges between −1 and 1 with its absolute value representing the probability of downward or upward onset (Fig. 2b, Fig. S5). We directly take the predicted *P* polarities from raw velocity waveforms for 38,518 well-located earthquakes as input data. We also measure *P*- and *S*-wave amplitudes from their arrivals and velocity waveforms

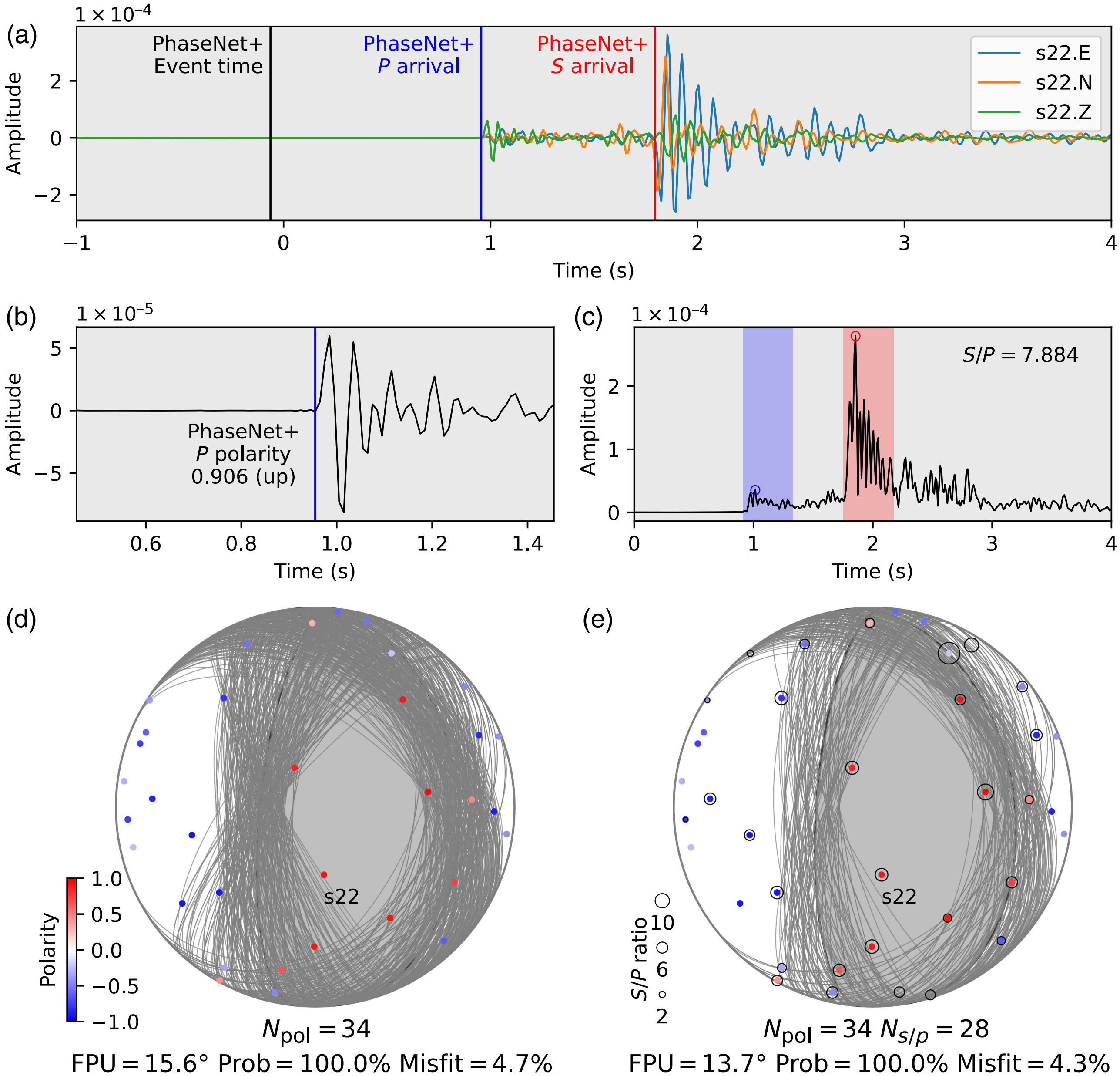

Figure 2. The determination of event time, phase arrivals, first-motion polarity, *S/P* amplitude ratio, and focal mechanism solutions for an M 1.53 event that occurred on 10 April 2016, 08:18:21.81 (UTC) is shown here as an example. (a) Three-component unfiltered velocity waveforms at station s22 are plotted together with the predicted event time, *P* and *S* arrivals by PhaseNet+. (b) The zoomed-in view of the vertical-component unfiltered velocity waveform and the predicted phase polarity by PhaseNet+. (c) The L2 norm of three-component filtered velocity waveforms and the windows used for measuring *P*- and *S*-wave amplitudes. Time in panels (a)–(c) is relative to the inverted event time after absolute location. (d) The focal mechanism was determined using only polarity data. (e) The focal mechanism was determined using both polarity and *S/P* ratio data. Stations color-coded by polarities and scaled by *S/P* ratios are projected into the lower focal sphere. FPU, fault-plane uncertainty; Misfit, polarity misfit percentage; *N*pol, number of polarities; *Ns/p*, number of *S/P* ratios; Prob, mechanism probability.

band-pass filtered between 1 and 15 Hz, a band preferred by previous studies (e.g., Hardebeck and Shearer, 2003). Although some regional studies used 1–10 Hz (e.g., Yang *et al.*, 2012), we slightly increase the upper limit considering that most recording stations are at local distances. We choose half the interval between *P* and *S* arrivals as the adaptive window length for measuring amplitudes. We omit this event waveform if the time-window length is less than 0.25 s and cap the maximum window length at 2 s. The time window is also shifted backward by 10% relative to the arrival to accommodate picking uncertainty. Finally, we obtain the L2 norm of three-component waveforms and take the maximum amplitudes in each

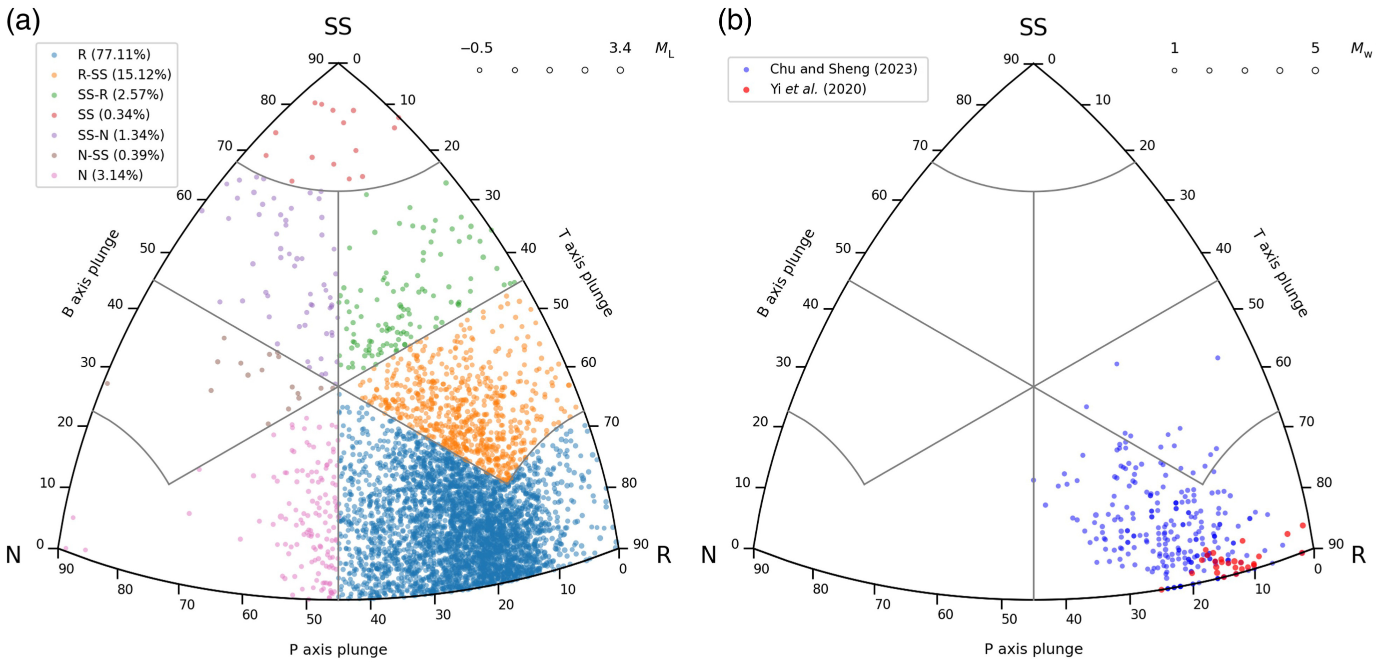

Figure 3. Faulting types of focal mechanisms determined from (a) this study and (b) previous studies. The dots with different colors in (a) denote different faulting types, and the percentages are shown in the legend. N, normal faulting; N-SS, normal faulting with strike-slip component; R, reverse faulting; R-SS, reverse faulting with strike-slip component; SS, strike-slip faulting; SS-N, strike-slip faulting with normal component; SS-R, strike-slip faulting with reverse component.

window as signal and noise amplitudes (Fig. 2c, Fig. S5). The SNR of *P* wave should be larger than 3, otherwise the corresponding *S/P* amplitude ratio would be discarded. The observed distribution of *S/P* ratios is compared with the theoretical distribution assuming the focal sphere is randomly sampled (Fig. S6). Because most earthquakes are spatially clustered (Fig. 1) and their focal mechanisms are not diverse enough, we are unable to estimate station corrections to resolve such discrepancies considering that the measurements at each station need to randomly sample the focal sphere.

We use SKHASH (Skoumal *et al.*, 2024), a format-flexible Python package based on the HASH algorithm (Hardebeck and Shearer, 2002), to compute focal mechanisms from *P* polarities and *S/P* ratios. One of its notable features is the ability to weight polarities, allowing it to directly take the polarities predicted by PhaseNet+ as input and weight them based on the prediction probabilities. Location uncertainties in lateral and vertical directions and two different velocity models (ZiVp1D and ZhouVp1D) are considered to allow for variable source–receiver azimuths and takeoff angles. The minimum number of required polarities is 8. The maximum allowed source–receiver distance, azimuthal gap, and takeoff angle gap are selected at 50 km, 90°, and 60°, respectively. We set the minimum allowed polarity weight from [0.1, 0.2, 0.3, 0.4, 0.5, 0.6] one by one with polarities with scores below this threshold being ignored to test the effect of this threshold on the results. The fraction of assumed bad polarities is 0.1 and the acceptable variation of *S/P* ratios on the logarithmic scale is 0.3. Through trying two velocity models and perturbing hypocenters, the focal mechanism of each earthquake is calculated for 30 trials, with each trial searching for acceptable solutions with a 5° grid angle. We use the default cutoff angle (45°) for computing focal mechanism probability and the default probability threshold (0.1) for multiples.

Results

Including *S/P* ratios in the inversion has derived more focal mechanisms with lower uncertainties than using only polarities (Fig. S7). This is because the number of acceptable solutions for an event decreases with more constraints, resulting in a more concentrated distribution around the preferred solution, as illustrated by the fitting results of an example earthquake (Fig. 2d–e). By including *S/P* ratios, the number of focal mechanisms with lower fault-plane uncertainties (<30°) and higher probabilities (>80%) has approximately doubled (Fig. S8a,b), whereas the polarity misfit also shows a slight increase (Fig. S8c,d). It indicates that focal mechanisms computed from both datasets of constraints may not differ a lot. We prefer the results combining *S/P* ratio constraints with a polarity threshold of 0.2, a value that gives the highest-quality (codes A and B) solutions when using only polarity data (Fig. S7). The final focal mechanism catalog has 20,740 solutions of varying qualities, accounting for ~54% of earthquakes from the hypocenter catalog. Proper filtering of the focal mechanism catalog to select high-quality solutions is an important step for the following interpretation. We consider only mechanism solutions assigned with codes A and B, which include 4399 mechanisms (Fig. S7). Although they account for only ~21.2% of the total number of focal mechanisms in the catalog, the amount is ~17 times the previous focal mechanism catalog derived from the same dataset through the waveform fitting method (Chu and Sheng, 2023), as more focal mechanisms of smaller earthquakes have been derived. Four earthquakes that appear in both catalogs are selected to compare the focal mechanism differences between the two catalogs. The angle differences are between 10° and 20°, suggesting a good consistency (Fig. S9).

We further classify the selected high-quality focal mechanisms into seven faulting types according to the orientations of the main axes (P, B, and T) and the Kaverina projection (Kaverina *et al.*, 1996; Álvarez-Gómez, 2019). The results show that about 92% of them are reverse faulting or reverse faulting accompanied by some strike-slip components (Fig. 3a). This is consistent with the results of Chu and Sheng (2023), in which they also determined most events as reverse faulting, except for a few with some strike-slip components (Fig. 3b). Focal mechanisms for even larger earthquakes (M > 3) from Yi *et al.* (2020) are all reverse-faulting types in comparison (Fig. 3b). These results indicate that faulting mechanisms may have become more dispersed for smaller earthquakes. One possible explanation may be the increased complexities of small-scale structures and stress fields responsible for many small earthquakes. Another explanation could be that the increased uncertainties for smaller earthquake focal mechanisms, resulting in the larger variability.

More focal mechanisms help illuminate the fault structures and stress fields at seismogenic depths with higher resolution. In this study, earthquakes are primarily distributed within two clusters, and their focal mechanism fault-plane uncertainties show no observable dependence on the locations. We use the focal mechanism's maximum pressure axis (P-axis) azimuth as a proxy for the direction of maximum horizontal compressive stress (e.g., Cheng *et al.*, 2023). P-axis

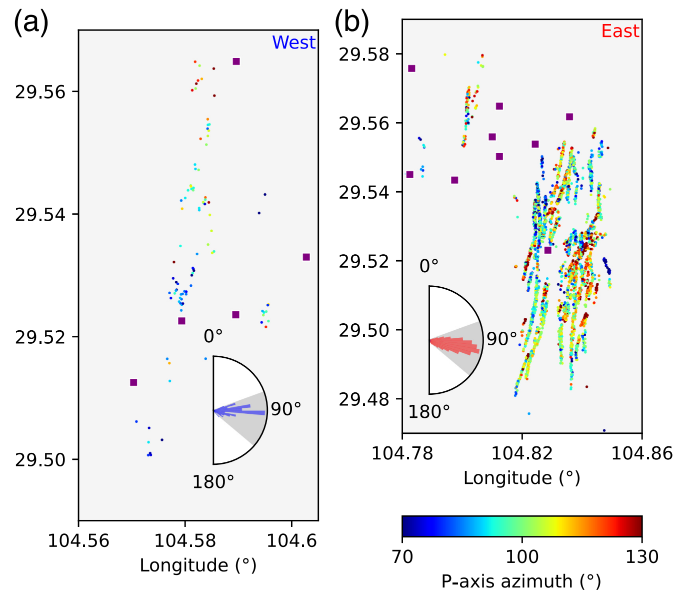

Figure 4. The spatial distribution of good-quality (classes A and B) focal mechanisms and their P-axis azimuths for the (a) west and (b) east clusters, positions for which have been marked in Figure 1. The purple squares show locations of hydraulic fracturing wells. Inset plots show the overall distribution of P-axis azimuth in each cluster. The shaded area corresponds to an azimuth range of [70, 130].

azimuths vary around 100° and fall mostly between 70° and 130° (insets in Fig. 4), consistent with the stress orientation of ~E20°S inverted by Chu and Sheng (2023). Regarding the eastern cluster, our results significantly improve the spatial resolution of resolved focal mechanisms (Fig. 4b). We find that P-axis azimuths are generally perpendicular to the delineated fault strikes, consistent with the major faulting types of reverse faulting (>77%). For example, the north–south- or north-northwest-trending faults tend to have smaller P-axis azimuths, but the north-northeast-trending faults usually correspond to larger P-axis azimuths. However, the existence of strike-slip components may lead to larger differences in P-axis azimuth, as shown in Figure S10. To better illustrate the spatial distribution of focal mechanisms of different types, we compute the scalar faulting types from the rakes of the two nodal planes following the method from Shearer *et al.* (2006). In both west and east clusters, except for the dominant reverse-faulting type (1), the strike-slip-faulting type (0) has appeared in different places (Fig. S11), indicating that earthquakes with some strike-slip components may have occurred more frequently than expected in the Weiyuan region.

Discussion

Homogeneity and heterogeneity of faulting mechanisms

Earthquake focal mechanisms present a large diversity in regions with varying tectonic regimes, such as in southern California (e.g., Rivera and Kanamori, 2002), related to the heterogeneous stress and strength in Earth's crust. However, the heterogeneity can decrease as the length scale decreases, with closely spaced earthquakes (<0.5–5 km) usually having similar focal mechanisms (Hardebeck, 2006). In general, our focal mechanism results support the homogeneity of earthquake faulting at shorter-length scales because the faulting types are dominantly reverse (Fig. 3) and their P axes exhibit a distinct concentrated distribution around 100° (Fig. 4). In summary, the faulting mechanisms of induced earthquakes in Weiyuan are primarily controlled by the prevalent north–south-trending faults and the regional tectonic stress, specifically the east–west compression (Chu and Sheng, 2023).

Recent high-resolution seismic catalogs reveal increasingly complex faulting geometry at smaller scales (e.g., Ross *et al.*, 2019; Shelly *et al.*, 2023). As a result of the complex faulting structures or the poroelastic stress perturbations (e.g., Lei *et al.*, 2017), subsurface stress features may become more heterogeneous. Apart from the general features in our results, we find that the heterogeneity of focal mechanisms seems nonnegligible given that the diversity of faulting types has gradually become larger with better catalogs (Fig. 3). Because high-quality focal mechanisms were chosen for our analysis, the maximum plane uncertainty is 35°, which indicates the larger angular differences observed between focal mechanisms of some earthquakes are real. Furthermore, similar diversity persists even when we focus on focal mechanisms with uncertainties below 20° (Fig. S12). The increase of diversity has also been observed in studies of larger earthquakes (Cheng *et al.*, 2024). One plausible explanation may be that smaller earthquakes with limited source dimensions are more easily influenced by stress perturbations, especially when the network of fractures or fault geometries is complex. The spatial variability of P-axis azimuths of our results remains obvious even if only focal mechanisms with lower uncertainties are shown (Fig. S13). It suggests that the local stress field has non-negligible variations at shorter-length scales. Shearer *et al.* (2024) have recently identified a well-recorded reverse-polarity earthquake pair (~115 m apart) with fault planes 10°–20° different in orientation, which is likely explained by the strong stress heterogeneity at short wavelengths.

In our catalog, a few normal-faulting events are present unexpectedly. We confirmed one of them by comparing the first motions at some surrounding stations to those from another adjacent reverse focal mechanism (Fig. 5). Because they occurred relatively close to each other and at similar depths, their reversed polarities suggest the opposing focal mechanisms. The occurrence of normal-faulting events may be attributed to the inversion of stress from compression to extension due to poroelastic effects or gravitational readjustment effects. Besides, it may also suggest a non-Andersonian stress state that principal stresses are neither vertical nor horizontal in some areas, where normal and reverse faulting can both occur on planes of different orientations. Because the ongoing fluid injection and gas extraction activities in the Weiyuan region could keep modulating the local stress field, the faulting mechanics of induced microseismic events may become more complex and variable. The timely and reliable determination of focal mechanisms of these smaller induced earthquakes may provide an effective tool to monitor the stress state near injection sites and thus mitigate seismic hazards.

Uncertainty of small earthquake focal mechanisms

Following previous studies (e.g., Yang *et al.*, 2012), we also examine the relationships between the fault-plane uncertainty and other parameters for the statistical characterization. Because larger earthquakes are more likely to be recorded by more stations, resulting in more constraints, their fault-plane uncertainties are generally smaller (Fig. S14). Likewise, the uncertainty also decreases with the number of used polarities or *S/P* ratios (Fig. S14). It is worth noting that such trends are less obvious or no longer exist when only larger earthquakes (e.g., $M > 0$) or enough constraints (e.g., >20 polarities) are considered, consistent with observations in Yang *et al.* (2012). The focal mechanism probability is defined as the percentage of acceptable solutions within the cutoff angle of preferred solutions, which is inversely proportional to the fault-plane uncertainty with a clear trend (Fig. S14). The fault-plane uncertainty does not show an obvious correlation with the polarity misfit or the average *S/P* ratio misfit, though larger misfit values seem to correspond to larger fault-plane uncertainties (Fig. S14). It remains challenging to derive reliable focal mechanism solutions for most small earthquakes. For example, focal mechanisms with quality C or D still account for the majority of results in our study and other regional studies (e.g., Cheng *et al.*, 2023). Except for increasing the density of seismic stations, it is important to seek more constraints, like

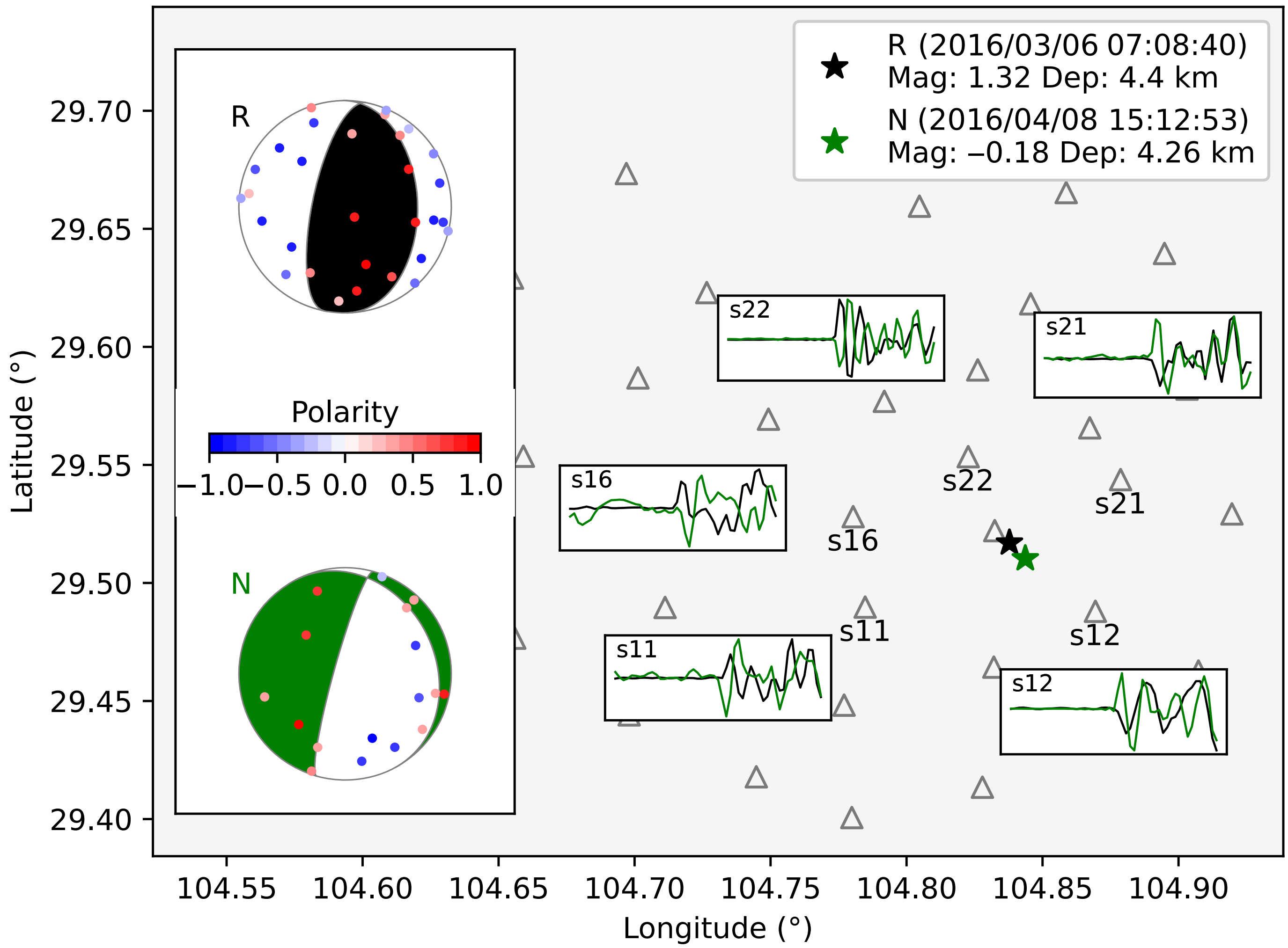

Figure 5. Two nearby earthquakes that have reverse (R) and normal (N) focal mechanisms, respectively, within the eastern cluster. The focal mechanism quality code for event R is A (FPU is ~15°), whereas the code for event N is B (FPU is ~30°). Opposite first-motion polarities are observed at stations surrounding them, providing strong evidence for the latter one being a normal focal mechanism.

correlation consensus polarities (e.g., Shelly *et al.*, 2016) or interevent amplitude ratios (e.g., Cheng *et al.*, 2024), to improve the accurate estimation of focal mechanisms. In the Weiyuan shale gas field, the injection of high-pressure fluid and opening of tensile cracks may have also resulted in volumetric components, demanding other methods (i.e., with non-double-couple components) and additional observations to constrain.

Conclusion

In this study, we have compiled an enhanced catalog of about 4400 good-quality focal mechanisms of induced earthquakes in Weiyuan, Sichuan, by leveraging a dense seismic array and a multitask deep learning model. Our high-resolution results show that (1) reverse rupturing on pre-existing north–south-trending faults is the primary faulting scenario, (2) earthquakes with most or part of strike-slip motions occur more frequently than previously observed and tend to be spatially clustered, (3) the variability of faulting mechanisms for smaller induced earthquakes may result from fault geometry complexity or stress field heterogeneity at short-length scales. By far, the seismogenic faults capable of producing larger earthquakes in the Weiyuan region are mainly oriented perpendicular to the tectonic compression direction. However, future hydraulic fracturing activities may further complicate the fractured networks and change the local stress field. Detailed characterization of small-scale earthquake faults, requiring dense near-field measurements and efficient processing tools, will become increasingly important for monitoring subsurface fault behavior and stress states to mitigate seismic hazards.

Data and Resources

The model predictions, the earthquake location, and focal mechanism catalogs are all available from Mendeley Data (doi: 10.17632/f6s2zsvddz.1). The model PhaseNet+ is available from https://github.com/AI4EPS/EQNet. The package GaMMA is available from https://github.com/AI4EPS/GaMMA. The package HYPOINVERSE is available from https://www.usgs.gov/software/hypoinverse-earthquake-location. The package FDTCC (https://github.com/MinLiu19/FDTCC) is used to calculate cross-correlation differential time. The package HypoDD is available from https://www.ldeo.columbia.edu/~felixw/hypoDD.html. The focal mechanism inversion package SKHASH is available from https://code.usgs.gov/esc/SKHASH. Data processing largely depends on ObsPy (https://docs.obspy.org). Figures are made using PyGMT (https://www.pygmt.org) and Matplotlib (https://matplotlib.org). All websites were last accessed in March 2025. The supplemental material includes additional figures that provide more details on the event detection and location results, the inverted focal mechanisms results, and the focal mechanism comparison and uncertainty analyses.

Declaration of Competing Interests

The authors acknowledge that there are no conflicts of interest recorded.

Acknowledgments

This study was supported by the National Natural Science Foundation of China (Grant Numbers U2139203 and 42325401), Hong Kong Research Grant Council Grants (Grant Numbers 14303721 and 14306122), Faculty of Science in The Chinese University of Hong Kong, and the CUHK Ph.D. IMPAC Award 2023-24. It benefited from discussions with Pengcheng Zhou and assistance from Minhan Sheng and Yukai Hu. The authors thank Editor-in-Chief Keith Koper, the anonymous associated editor(s), and the two anonymous reviewers for their helpful comments and suggestions that greatly improved the article. The authors also thank Managing Editor Tom Green for the assistance.

References

Álvarez-Gómez, J. A. (2019). FMC-earthquake focal mechanisms data management, cluster and classification, *SoftwareX* **9,** 299–307.

Cheng, Y., R. Bürgmann, and R. M. Allen (2024). 3D architecture and complex behavior along the simple central San Andreas fault, *Nat. Commun.* **15,** no. 1, 5390.

Cheng, Y., E. Hauksson, and Y. Ben-Zion (2023). Refined earthquake focal mechanism catalog for southern California derived with deep learning algorithms, *J. Geophys. Res.* **128,** no. 2, e2022JB025975, doi: 10.1029/2022JB025975.

Chu, R., and M. Sheng (2023). Stress features inferred from induced earthquakes in the Weiyuan shale gas block in southwestern China, *J. Geophys. Res.* **128,** no. 2, e2022JB025344, doi: 10.1029/2022JB025344.

Hardebeck, J. L. (2006). Homogeneity of small-scale earthquake faulting, stress, and fault strength, *Bull. Seismol. Soc. Am.* **96,** no. 5, 1675–1688.

Hardebeck, J. L., and P. M. Shearer (2002). A new method for determining first-motion focal mechanisms, *Bull. Seismol. Soc. Am.* **92,** no. 6, 2264–2276.

Hardebeck, J. L., and P. M. Shearer (2003). Using S/P amplitude ratios to constrain the focal mechanisms of small earthquakes, *Bull. Seismol. Soc. Am.* **93,** no. 6, 2434–2444.

Kaverina, A. N., A. V. Lander, and A. G. Prozorov (1996). Global creepex distribution and its relation to earthquake-source geometry and tectonic origin, *Geophys. J. Int.* **125,** no. 1, 249–265.

Klein, F. W. (2002). User's guide to HYPOINVERSE-2000, a Fortran program to solve for earthquake locations and magnitudes, *U.S. Geol. Surv. Open-File Rept. 02-171*.

Lei, X., D. Huang, J. Su, G. Jiang, X. Wang, H. Wang, X. Guo, and H. Fu (2017). Fault reactivation and earthquakes with magnitudes of up to M_w 4.7 induced by shale-gas hydraulic fracturing in Sichuan Basin, China, *Sci. Rep.* **7,** no. 1, 7971, doi: 10.1038/s41598-017-08557-y.

Li, J., H. Zhang, H. Kuleli Sadi, and M. Toksoz Nafi (2011). Focal mechanism determination using high-frequency waveform matching and its application to small magnitude induced earthquakes, *Geophys. J. Int.* **184,** no. 3, 1261–1274.

Rivera, L., and H. Kanamori (2002). Spatial heterogeneity of tectonic stress and friction in the crust, *Geophys. Res. Lett.* **29,** no. 6, 12-1–12-4.

Ross, Z. E., B. A. Idini, Z. Jia, O. L. Stephenson, M. Zhong, X. Wang, Z. Zhan, M. Simons, E. Fielding, and S.-H. Yun, *et al.* (2019). Hierarchical interlocked orthogonal faulting in the 2019 Ridgecrest earthquake sequence, *Science* **366,** no. 6463, 346–351.

Ross, Z. E., M. A. Meier, and E. Hauksson (2018). P wave arrival picking and first-motion polarity determination with deep learning, *J. Geophys. Res.* **123,** no. 6, 5120–5129.

Shearer, P. M., G. A. Prieto, and E. Hauksson (2006). Comprehensive analysis of earthquake source spectra in southern California, *J. Geophys. Res.* **111,** no. B6, doi: 10.1029/2005JB003979.

Shearer, P. M., N. Senobari Shabikay, and Y. Fialko (2024). Implications of a reverse polarity earthquake pair on fault friction and stress heterogeneity near Ridgecrest, California, *J. Geophys. Res.* **129,** no. 11, e2024JB029562, doi: 10.1029/2024JB029562.

Shelly, D. R., J. L. Hardebeck, W. L. Ellsworth, and D. P. Hill (2016). A new strategy for earthquake focal mechanisms using waveform-correlation-derived relative polarities and cluster analysis: Application to the 2014 Long Valley Caldera earthquake swarm, *J. Geophys. Res.* **121,** no. 12, 8622–8641.

Shelly, D. R., R. J. Skoumal, and J. L. Hardebeck (2023). Fracture-mesh faulting in the swarm-like 2020 Maacama sequence revealed by high-precision earthquake detection, location, and focal mechanisms, *Geophys. Res. Lett.* **50,** no. 1, e2022GL101233, doi: 10.1029/2022GL101233.

Sheng, M., R. Chu, Z. Peng, Z. Wei, X. Zeng, Q. Wang, and Y. Wang (2022). Earthquakes triggered by fluid diffusion and boosted by fault reactivation in Weiyuan, China due to hydraulic fracturing, *J. Geophys. Res.* **127,** no. 5, e2021JB022963, doi: 10.1029/2021JB022963.

Skoumal, R. J., J. L. Hardebeck, and P. M. Shearer (2024). SKHASH: A python package for computing earthquake focal mechanisms, *Seismol. Res. Lett.* **95,** no. 4, 2519–2526.

Waldhauser, F., and W. L. Ellsworth (2000). A double-difference earthquake location algorithm: Method and application to the northern Hayward fault, California, *Bull. Seismol. Soc. Am.* **90,** no. 6, 1353–1368.

Yang, H., P. Zhou, N. Fang, G. Zhu, W. Xu, J. Su, F. Meng, and R. Chu (2020). A shallow shock: The 25 February 2019 ML 4.9 earthquake in the Weiyuan shale gas field in Sichuan, China, *Seismol. Soc. Am.* **91,** no. 6, 3182–3194.

Yang, W., E. Hauksson, and P. M. Shearer (2012). Computing a large refined catalog of focal mechanisms for southern California (1981–2010): Temporal stability of the style of faulting, *Bull. Seismol. Soc. Am.* **102,** no. 3, 1179–1194.

Yi, G., F. Long, M. Liang, M. Zhao, and S. Wang (2020). Geometry and tectonic deformation of seismogenic structures in the Rongxian-Weiyuan-Zizhong region, Sichuan Basin: Insights from focal mechanism solutions, *Chin. J. Geophys.* **63,** no. 9, 3275–3291.

Zhang, W., R. Guo, L. Ji, H. Yang, K. Dai, J. Zi, and H. Sun (2024). Shallow reverse moderate earthquakes in the Weiyuan Shale Gas Field, Sichuan Basin, China, related to hydraulic fracturing, *Seismol. Res. Lett.* doi: 10.1785/0220230375.

Zhou, P., W. L. Ellsworth, H. Yang, Y. J. Tan, G. C. Beroza, M. Sheng, and R. Chu (2021). Machine-learning-facilitated earthquake and anthropogenic source detections near the Weiyuan Shale Gas Blocks, Sichuan, China, *Earth Planet. Phys.* **5,** no. 6, 532–546.

Zhu, W., and G. C. Beroza (2019). PhaseNet: A deep-neural-network-based seismic arrival-time picking method, *Geophys. J. Int.* **216,** no. 1, 261–273.

Zhu, W., J. Song, H. Wang, and J. Münchmeyer (2025). PhaseNet+: End-to-end earthquake monitoring using a multitask deep learning model, arXiv preprint, available at https://agu.confex.com/agu/agu24/meetingapp.cgi/Paper/1526798 (last accessed March 2025).

Zhu, W., I. W. McBrearty, S. M. Mousavi, W. L. Ellsworth, and G. C. Beroza (2022). Earthquake phase association using a Bayesian Gaussian mixture model, *J. Geophys. Res.* **127,** no. 5, e2021JB023249, doi: 10.1029/2021JB023249.

Zi, J., H. Yang, J. Su, and L. Chen (2023). Structural constraints of induced earthquakes in the Weiyuan Shale Gas Field revealed by high-resolution body-wave tomography and earthquake relocation, *Tectonophysics* **864,** 230007, doi: 10.1016/j.tecto.2023.230007.

Zi, J., Y. Yang, H. Yang, and J. Su (2025). The 11-month precursory fault activation of the 2019 ML 5.6 earthquake in the Weiyuan shale gas field, China, *Commun. Earth Environ.* **6,** no. 1, 175, doi: 10.1038/s43247-025-02151-1.

Manuscript received 24 January 2025
Published online 8 May 2025